RESEARCH ARTICLE | NOVEMBER 06 2015

Study of ablation and implosion stages in wire arrays using coupled ultraviolet and X-ray probing diagnostics FREE

A. A. Anderson; V. V. Ivanov ; A. L. Astanovitskiy; D. Papp; P. P. Wiewior; O. Chalyy

Check for updates

CHORUS

CrossMark

View Online

Export Citation

Physics of Plasmas

Features in Plasma Physics Webinars

Register Today!

AIP Publishing

AIP Publishing

Study of ablation and implosion stages in wire arrays using coupled ultraviolet and X-ray probing diagnostics

A. A. Anderson,[1] V. V. Ivanov,[1] A. L. Astanovitskiy,[1] D. Papp,[1,2] P. P. Wiewior,[1] and O. Chalyy[1]

[1]*University of Nevada Reno, Reno, Nevada 89557, USA*
[2]*ELI-ALPS, ELI-Hu Nkft., H-6720 Szeged, Hungary*

Star and cylindrical wire arrays were studied using laser probing and X-ray radiography at the 1-MA Zebra pulse power generator at the University of Nevada, Reno. The Leopard laser provided backlighting, producing a laser plasma from a Si target which emitted an X-ray probing pulse at the wavelength of 6.65 Å. A spherically bent quartz crystal imaged the backlit wires onto X-ray film. Laser probing diagnostics at the wavelength of 266 nm included a 3-channel polarimeter for Faraday rotation diagnostic and two-frame laser interferometry with two shearing interferometers to study the evolution of the plasma electron density at the ablation and implosion stages. Dynamics of the plasma density profile in Al wire arrays at the ablation stage were directly studied with interferometry, and expansion of wire cores was measured with X-ray radiography. The magnetic field in the imploding plasma was measured with the Faraday rotation diagnostic, and current was reconstructed. © *2015 AIP Publishing LLC*. [http://dx.doi.org/10.1063/1.4934980]

I. INTRODUCTION

Wire array Z pinches are the most powerful laboratory source of soft X-rays.[1–4] This makes them a powerful platform for inertial confinement fusion research and other high energy plasma applications. Instabilities form early in Z-pinch plasma, and these instabilities are thought to be the primary factor in determining the power of this X-ray production. Reducing the growth of instabilities has been shown to increase the intensity of X-ray radiation.[1–5] Instabilities arise at the ablation stage,[6] develop during implosion,[7] and are transferred to the structure of the Z pinch. Kink and sausage instabilities strongly impact the pinch at the stagnation stage.[8,9] Therefore, the structure and dynamics of the early plasma stages are of importance for the formation of the Z pinch.

In the ablation stage of the Z pinch, fine metal wires are subjected to the rising current created from pulse power generators. This current pulse causes surface breakdown of wires. Plasma arises on the surface of the wire and undergoes ohmic heating. A complicated "core-corona" structure of plasma is formed in wires at the ablation stage.[6,10] The current creates a global magnetic field, and the resulting $\mathbf{J} \times \mathbf{B}$ force pulls the corona plasma towards the center of the wire array. The ablated plasma produces a precursor plasma column in the center of the array. The wire cores are still cold and stay in a dense non-plasma condition.[11–14] Plasma is continually ablated off the wire core until breaks arise. The implosion stage begins when the bulk of the mass of the wire is imploded towards the center of the Z pinch. Instabilities imprinted to the imploding plasma impact the Z pinch.

Side-on and end-on laser diagnostics at the wavelengths of 532 nm and 355 nm were used for the investigation of the ablating plasma jets, formation of the precursor, and general implosion dynamics.[14–16] However, both the core and the corona plasma at the ablation stage are opaque for laser probing in the optical range. Optical diagnostics cannot reveal the structure of ablating wires or dense imploding plasma. Laser diagnostics at the wavelength of 266 nm have better penetration ability. Previous studies with ultraviolet (UV) diagnostics focused on the stagnated Z pinch[8,9] but have never been used for detailed investigation of plasma of ablating wires.

X-ray backlighting can be used to study dense plasma. Wire cores with a high mass density have been studied using x-ray imaging backlighting by X-pinches.[11–13,17] X-pinch point-projection radiography allowed observation of the fine structure of the wire core with high spatial resolution. A multiphase foam-like structure of the expanded core was seen in X-pinch wires.[11] Disc-like structures in the wire cores of cylindrical wire arrays were reported in Ref. 12. Knowing the core and corona fine structure helps to understand the development of plasma instabilities which impacts the imploding plasma and imprints later to the Z pinch. However, the coronal plasma of light elements like Al is transparent to the x-ray backlighting in the keV range. The coronal plasma was studied only in tungsten wires due to the higher absorption of x-rays in the plasma of high-atomic-number elements.[18,19] The electron temperature of coronal plasma in the ablating wire was measured, $T_e = 5-25$ eV using absorption lines in Al star wire arrays[20] and 2-wire loads.[21]

The laser-based x-ray radiography has been used widely in laser plasma interaction studies. The laser-based radiography was applied to the Z pinch at the 20-MA Z machine[22] where it was fielded as a diagnostic to measure the mass distribution of imploding material during the implosion stages in multi-wire arrays.

In this paper, we study plasma dynamics and parameters during the ablation stage using coupled UV laser diagnostics which include a three-channel polarimeter and two-frame interferometer and x-ray radiography. Wire arrays used in the experiments were Al cylindrical, linear, and three-ray star

configurations, 2 cm tall with wires 15–25 μm in diameter, and total arrays masses of 27–140 μg/cm. The laser probing at the wavelength of 266 nm allows for the direct measurement of electron plasma density in the wire plasma column and imploding plasma in cylindrical and linear arrays. Dynamics of the corona plasma density distribution in Al cylindrical wire arrays at the ablation stage were studied with two-frame interferometry. Dynamics of the core size in cylindrical and star arrays was studied with the laser-based imaging radiography using the Leopard laser in the Nevada Terawatt Facility (NTF) at the University of Nevada, Reno (UNR). Current in the imploding plasma of the Al star wire array was reconstructed with the Faraday rotation diagnostics. Coupled laser and X-ray probing diagnostics provide data for a wide range of density from plasma to solid in one shot of the 1 MA Zebra generator.

II. EXPERIMENTAL SETUP AND PLASMA DIAGNOSTICS

Experiments were performed at the 1-MA Zebra pulse power generator, at the NTF. The Zebra generator produces a pulse with a rise time of 90 ns from 10% to 90% of peak current at an impedance of 1.9 Ω. A current pulse profile is measured by three B-dots installed on the anode plate. "Core" X-ray diagnostics include calibrated, filtered X-ray diodes (XRD) and photo-conducting detectors (PCD) for measuring the temporal profile of the X-ray emission from the Z-pinch, a bare Ni bolometer for measuring total radiating energy in the spectral region from 10 eV to 4–5 keV, a six-frame pinhole camera for imaging in the keV range, and time integrating spectrometer in the range of 4–15 Å for measuring the electron plasma temperature and density in the stagnated Z pinch.[22]

Laser diagnostics include probing of the Z-pinch with wavelengths of 532 nm and 266 nm along three azimuthal directions. UV laser probing uses the 4th harmonic of a Nd:YAG laser and is used for shadowgraphy, interferometry, and the Faraday rotation diagnostic. For laser probing of dense Z-pinch plasmas, the limiting factor for effectiveness of the probing beam is often the inverse bremsstrahlung or free-free absorption. The inverse bremsstrahlung absorption coefficient is given by the formula[23]

$$\gamma = 8.73 \times 10^{-30} \lambda^2 \frac{n_e^2 Z \Lambda}{T_e^{\frac{3}{2}} \left(1 - \frac{n_e}{n_c}\right)^{\frac{1}{2}}}, \qquad (1)$$

where λ is the wavelength of the probing beam, n_e is the electron density, n_c is the critical density of the plasma, T_e is the electron temperature, Z is the ion charge, and Λ is the Coulomb logarithm. By decreasing the wavelength of the probing laser, we can significantly decrease the absorption, allowing us to probe denser plasmas. This has motivated the development of UV laser probing at the wavelength of 266 nm at the NTF.[8,24]

The electron density of the plasma is typically measured with interferometry.[23] A regular Mach-Zehnder interferometer is too sensitive to measure the plasma densities in our

experiments due to the high phase shift in the dense plasmas. A differential air-wedge interferometer[25] with lower sensitivity can measure the higher plasma density.[26] Processing of the differential interferogram needs an undisturbed fringe in the interferogram to give the reference point for the analysis. The absolute phase shift is then reconstructed from the differential phase shift. Once the phase shift is determined, electron density profiles can be reconstructed with Abel inversion.[26]

To study the plasma dynamics during the ablation stage, 2-frame interferometry is used. The laser is split into two polarizations, one which branches off into an optical delay line before rejoining the original optical path. The two pulses with different delays are separated at two CCD cameras by polarizers. This allows us to probe the same experimental shot and measure the electron density at two time frames.

The experimental setup for the Faraday rotation diagnostic, shown in Fig. 1, uses a three-channel UV polarimeter.[26] The polarimeter takes shadowgram, interferogram, and Faraday images at one moment in time. Before the vacuum chamber of the Zebra generator, a high-contrast Glan prism polarizes the incident laser beam at 266 nm. A thin crystal wedge is set-up after the vacuum chamber and rotated a small angle α_0 with respect to the polarization angle for the Glan prism. This rotation allows one to determine the direction of the magnetic field, based on the direction of the Faraday rotation. The crystal wedge splits the orthogonal polarizations into two angularly separated beams. One beam goes to the shadowgraphy channel, and the second goes to the Faraday rotation channel. The shadowgraphy channel is split off to an interferometry channel using an air-wedge shearing interferometer. A three-lens beampath relays an image of plasma to three CCD cameras with the same magnification. Spatial resolution of UV diagnostic is 15 μm in this configuration.

X-ray radiography is obtained by backlighting the wire array with X-ray emissions produced by the Leopard laser striking a target material within the vacuum chamber of the Zebra generator.[27] The Leopard laser at NTF is a 1057 nm Ti:Sa and Nd:glass laser capable of operating in two modes, one a "short pulse" mode with 0.35 ps pulse duration and 12 J of energy or the "long pulse" mode featuring a 0.6 ns laser pulse with up to 40 J of energy.[28] X-ray imaging with bent spherical crystals allows for high resolution, time-
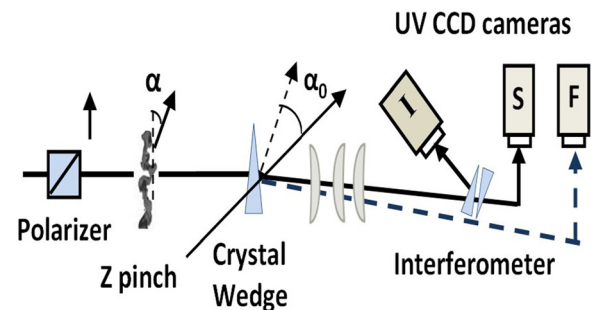

FIG. 1. Schematic of 3-channel polarimeter used in Faraday rotation diagnostic. Three images are captured on CCD cameras for interferometry (I), shadowgraphy (S), and Faraday images (F).
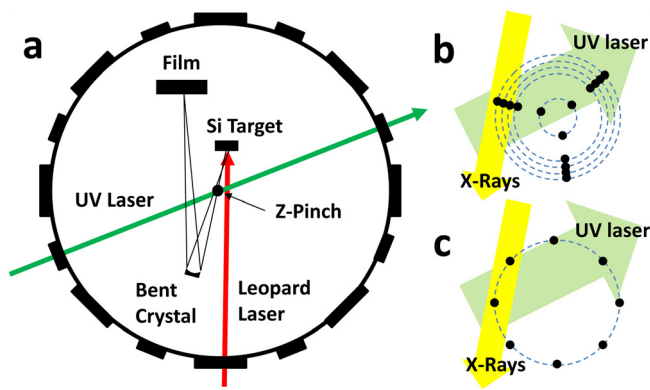
FIG. 2. (a) Experimental schematic for simultaneous 266 nm laser probing and x-ray backlighting using the 6.65 Å Si He$_\alpha$ spectral line produced by hitting a Si Target with the Leopard laser. Experiments were performed by star wire array (b) and cylindrical wire array (c) with 18 mm diameters.

resolved measurements of the core structure of wires seen during the ablation stage.[29] In our experimental set-up, a spherically bent quartz crystal, cut 1011 is tuned on the 6.65 Å He-α spectral line of the Si plasma. This gives a Bragg angle of 83.9° or 6.1° from the axis perpendicular of the center of the crystal. At this angle, $\sin(\theta)$ is 0.994, and so the optical aberration caused by the astigmatism is small. A low spectral selection bandwidth of 10^{-4} to 10^{-3} allows one to the backlighting radiation from the background emissions of the Z pinch.

The experimental set-up for X-ray imaging coupled with UV laser probing is shown in Figure 2(a). There is a lead shield blocking the film cassette from directed and stray X-rays emitting from the Z pinch. Two collimators geometrically block additional background radiation and plasma debris from the spherically bent crystal and film cassette. In addition, a Be filter is placed in front of the spherically bent crystal, which allows keV X-rays to pass through unhindered but acts as a screen for soft X-rays and debris that is not blocked by the collimator. With the small angle of incidence for the X-rays on the crystal, the incoming and outgoing X-rays pass through the same filter. The object and image distances are at 20 cm and 33 cm, respectively. Directions of X-ray imaging and UV laser probing are shown for two loads, a 3-ray star wire array in Fig. 1(b) and a cylindrical wire array in Fig. 1(c).

Experiments were performed with 2 cm tall Al cylindrical, linear, and star wire arrays. Star wire arrays consist of wires aligned along linear "rays" extending radially from the axis. In linear arrays, wires are placed along a line. Cylindrical arrays have all wires located at a single diameter.

The three types of loads implode in different manners. In cylindrical arrays, all wires implode to the center of the array in a similar manner and time frame. In star arrays, implosion begins on the edge wires, cascades from wire to wire, and sweeps all material to the center. During the ablation and implosion stages, wires are at different stages of development depending on their location. In linear arrays, implosion bubbles pass through all the wires and start the generation of the X-ray pulse when most material is still at the initial position. The secondary implosion of the

non-imploded material plays an important role in the generation of the long X-ray pulse.

III. EXPERIMENTS

A. Study at the ablation and implosion stages in wire arrays with UV interferometry

Wire arrays used in the experiments were Al cylindrical, linear, and three-ray star configurations,[30] 2 cm tall with wires 15–25 μm in diameter, and total arrays masses of 27–140 μg/cm. Figure 3 shows a shadowgram and interferograms of ablating wires from an 8-wire cylindrical wire-array Z-pinch, 16 mm in diameter. Images (a) and (b) are taken in laser frame 1 at 45 ns before the maximum of the X-ray pulse. Image (c) is recorded 7 ns later in the second laser frame. Figure 3(a) is the shadowgram of the plasma columns of two ablating wires, and Figures 3(b) and 3(c) are the accompanying interferometric images. Note that the left wire in shadowgram (a) still has a dense wire core, visible in both wires, but for the wire on the right in the shadowgram the dense wire core is blurred and disrupted. The diameter of the plasma columns is 0.2–0.25 mm in shadowgram (a). The core is seen in the left wire and absent in the right one in both interferograms. The wire core of the left wire is distorted in the second-frame interferogram (c) with disruption shown by the arrow. The wire core is presumably converted to plasma in the right wire in Fig. 3.

In Figure 4, the right wire from Fig. 3 is selected for the interferometric measurements. Figure 4(a) shows a shadowgram of the wire taken simultaneously with the interferometric image (b) in laser frame 1. Figure 4(c) shows the interferometric image of the same wire in laser frame 2, 7 ns later in time from laser frame 1. For both Figs. 4(b) and 4(c), pre-shot reference images show the location of the wire to be at the center of the fringe structure. Some azimuthal symmetry can be seen even in the irregular surface structure of the wire. A non-disturbed fringe is necessary for processing the differential interferogram. We used the outer half of the outer-most wire which is always measurable in the interferogram. The electron density on another side of the wire is not acceptable for processing due to the ablation plasma jets streaming to the center of the wire array. The technique used in our analysis involved assuming cylindrical symmetry, and
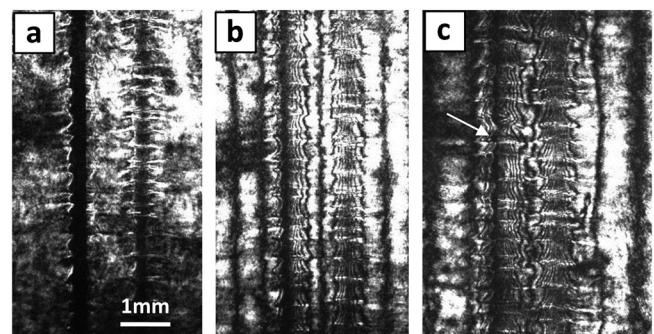

FIG. 3. The ablation stage in a cylindrical array with eight 12.7 μm Al wires, shot 2883. (a) and (b) The shadowgram and interferogram taken in laser frame 1, respectively. (c) The interferogram taken 7 ns later in laser frame 2.
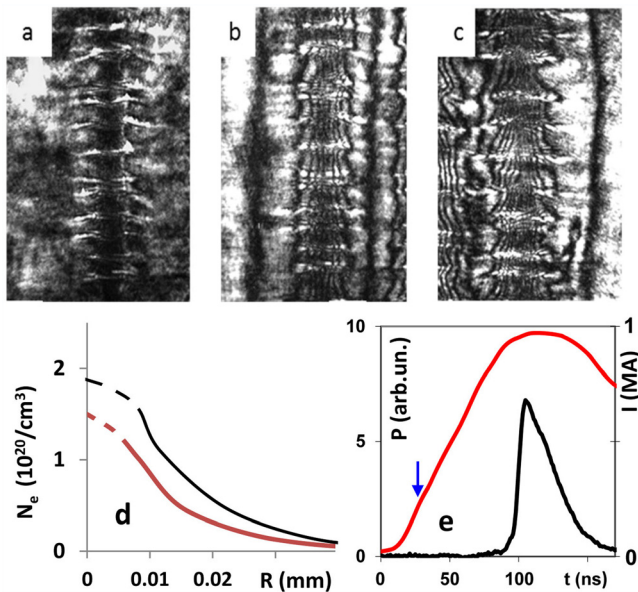
FIG. 4. (a) Shadowgram and (b) interferogram in laser frame 1 taken simultaneously in the cylindrical 8-wire array in shot 2883. (c) Interferogram in laser frame 2 taken 7 ns later after image (b). (d) Calculated electron density for frame 1 (red line) and frame 2 (blue line). Dashed lines show approximated $n_e(r)$. (e) Timing diagram, showing laser timing of images (a) and (b) (blue arrow) to the current pulse (red line) and x-ray pulse (black line).

using Abel inversion to derive the electron density $n_e(r)$ as a function of radius for the plasma column[26]

$$n_e(r) = \frac{2m_e c^2}{e^2 \lambda} \int_y^{R_0} \frac{d\varphi(y)}{dy} \frac{dy}{\sqrt{y^2 - r^2}} dr, \qquad (2)$$

where λ is the wavelength of the beam, y is the distance between the ray and the pinch axis, and R_0 is the pinch radius. Abel transform requires that the phase profile as a function of distance y and its first derivative are continuous and smooth.

In Figure 4(d), the electron density calculated with Abel-inversion is shown for the 2 frames of interferometry in images (b) and (c). The radius of the plasma column is determined from interferograms. The shift of the interferometer is calculated from the reference interferogram. The peak electron density measured for two frames is 1.2×10^{20} and $1.6 \times 10^{20} \, \text{cm}^{-3}$ near the center, and the electron density quickly drops off further from the wire core. This represents the direct measurement of the electron density of the wire plasma column in a Z pinches using interferometry.

The calculated electron density $n_e(r)$ allows for the calculation of total mass of plasma in the ablating wire. For these calculations, curves $n_e(r)$ were approximated to the axis by dashed lines as it is shown in Fig. 4(d). Previous measurements with absorption spectroscopy showed that the electron temperature of Al wire-array plasma at the ablation stage is distributed in the range of 5–25 eV.[20] We assume an electron temperature of 20–25 eV near the end of the ablation stage and the ionic charge of Z = 5–6. The mass of material in the plasma column was integrated using the radial distribution of the electron density from the diagram in Fig. 4 and an appropriate ionic charge. Calculations show that the interferometry in frame 2 measures ~72% of the total mass of
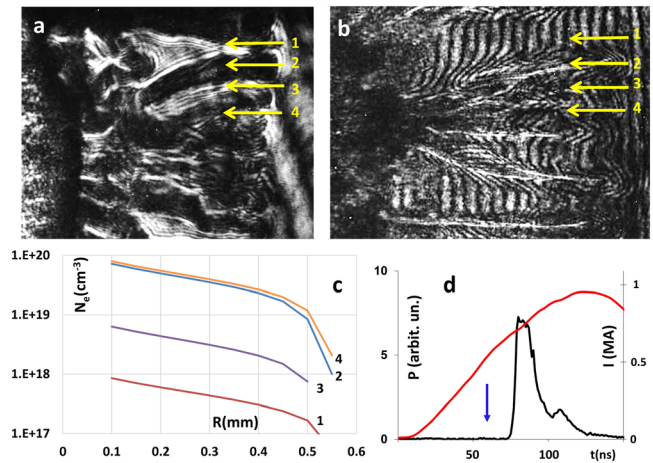

FIG. 5. (a) Shadowgram and (b) interferogram taken simultaneously in shot 2816 with a 10-wire Al linear load. (c) Calculated electron density for lineouts shown in (a). (d) Timing diagram, showing laser timing (blue arrow) to the current pulse (red line) and x-ray pulse (black line).

the wire if Z = 6. This estimation does not take into account a distribution of the real temperature and ionization stage. The wire core can include small non-plasma portions, not seen by interferometry, and plasma ablated to the center of the pinch is not taken into account in this estimation. Integration of plasma density in interferogram (b) shows that 36% of the total mass of the wire is contained in the plasma column in frame 1 if Z = 5. In this case, the rest of the mass is mostly contained in the non-plasma core.

The implosion stage in wire arrays was studied with interferometry and shadowgraphy. Figure 5(a) shows a shadowgram of an Al linear 10-wire load with 12 μm wires at the beginning of implosion. The outermost wire on the right side of the image had formed plasma bubbles which imploded towards the next inner wires. Imaged on the right side of the shadowgram is the trailing mass left behind by these imploding plasma bubbles. These fingers of trailing mass were studied along with the gaps in order to determine the electron density distribution in the trailing plasma, which implode later. Four locations were studied, two directly on the fingers of trailing mass, and two in the gaps in between. Figure 5(c) shows the calculated electron density profile for these 4 regions using Abel inversion. The fingers of plasma have a peak electron density of $10^{20} \, \text{cm}^{-3}$. The two gaps between fingers have the electron density 10^{19} and $10^{18} \, \text{cm}^{-3}$, revealing that the gaps contain some plasma. This plasma between the fingers of trailing mass provides a continuous current path after the initial implosion. This would then provide the mechanism for the implosion of the remaining trailing mass during stagnation. Z pinch X-ray emission can have more energy than is accounted for using kinetic energy and Spitzer resistive heating.[31,32] Re-implosion of this trailing mass may account for some of the enhanced plasma heating.[33]

B. Study of magnetic fields in the imploding plasma

A UV Faraday rotation diagnostic at the wavelength of 266 nm was used to study the magnetic field and determine the current distribution in the imploding plasma of wire

arrays. Faraday diagnostics can be used to measure the local magnetic field strength when coupled with interferometric data. The 3-ray star load consisted of 12 Al wires, 10 μm in diameter, placed on diameters of 16/12/8/5 mm. Figure 6 shows an image of the (a) shadowgram and (b) complementary Faraday image during the implosion stage of a star wire array. Current in the plasma can be identified by lightening in the left side and darkening in the right side of plasma columns in the Faraday image due to the magnetic field being in opposite directions in these areas. A line in Fig. 3 shows the direction of reconstruction of the magnetic field. The Faraday rotation angle is calculated from the Faraday image, shadowgram, and reference images. All images were spatially co-aligned. Using reference images helps to avoid measuring the transmission of filters in three channels of the polarimeter. The rotation angle β in plasma was calculated by the formula

$$\mathrm{Sin}(\beta + \beta_0) = \sqrt{\frac{I_F}{I_S} \cdot \frac{I_{Sref}}{I_{Fref}} \left(\mathrm{Sin}^2(\beta_0) + K \right) - K}, \quad (3)$$

where I_F, I_S, I_{Fref}, and I_{Sref} are intensities in the Faraday CCD image, shadowgram, reference Faraday image, and reference shadowgram along the directions of data processing, β_0 is the mismatched angle of polarizers, and $K = 10^{-4}$ is a contrast of the polarimeter.

The electron density up to 0.6×10^{20} cm^{-3} was measured in interferogram (c). After extracting the Faraday rotation angle from the Faraday image and calculating the electron density profile from an accompanying interferogram, the magnetic field strength can be reconstructed. The magnetic field is given as

$$B(r) = \frac{r}{n_e(r)} \frac{2\pi \cdot m_e^2 c^2}{e^2 \lambda^2} \int_r^{R_0} \frac{d}{dy} \frac{\beta(y)}{y} \frac{dy}{\sqrt{y^2 - r^2}}, \quad (4)$$

where $B(r)$ is the magnetic field, and β is the Faraday rotation angle. The magnetic field can then be used to create a simple model of the local electric current. The rotation angle $\beta(r)$ and plasma electron density $N_e(r)$ are approximated by smooth lines to improve the accuracy of the reconstruction procedure. The Faraday rotation diagnostic is not applicable, due to strong refraction and absorption in the region at the small radius. The error of reconstruction grows strongly at low electron density and rotation angle on the region at the larger radius due to the poor small/signal ratio. The total error of reconstruction of the current is estimated $\pm 20\%$.

Figure 6(d) shows the reconstructed magnetic field strength profile that has been created using this method (black line). A simple model of a 0.6 MA cylindrically uniform current with a constant density, with radius of 0.9 mm (dashed line) is also shown. The plasma column on the right in images (a)–(c) represents two overlapping plasma columns from the 3-ray star wire array configuration. Assuming 0.94 MA of current at this moment is evenly distributed between the three plasma columns, roughly 0.6 MA would located in the double column on the right in Fig. 3(b). The magnetic field strength and current in the imploding plasma columns are consistent with expected results. We note Figure 6(c) shows the direct measurement of the magnetic field and current in plasma of the 1 MA wire array Z pinch at the implosion stage.

C. Laser-based X-ray imaging of wire cores in the arrays

A laser-based X-ray imaging diagnostic is applied for investigation of the dense core of wires at the ablation stage. The dense cores are backlit by the 6.65 Å X-ray pulse from the Si laser-produced plasma and imaged using the spherically bent quartz crystal, cut 1011. Experiments were performed using X-ray imaging coupled with laser shadowgraphy and interferometry at the wavelength of 266 nm. Figures 7(a) and 7(b) show ranges in the wire plasma available for the interferometry and X-ray backlighting in one shot. In Figure 7(a), the diameter of the dense wire core is measured with X-ray imaging, and the electron density is measured with interferometry, using the methods listed in Section III A above. The interferometry measures the electron plasma
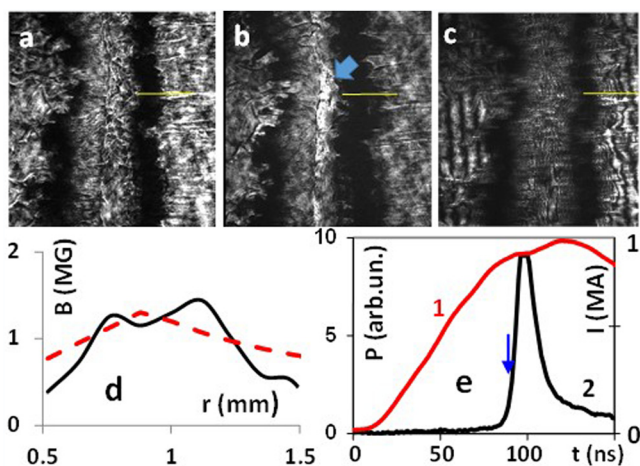

FIG. 6. (a) Shadowgram, (b) Faraday image, and (c) interferogram taken simultaneously during the implosion stage in the 3-ray 12-wire Al star array in shot 2947. The arrow highlights area of lightening from the Faraday effect. (d) Calculated magnetic field (solid line) and the magnetic field of a 0.6 MA cylindrically uniform current with radius 0.9 mm (dashed line). (e) Timing diagram with a laser pulse (arrow) current pulse (1) and the keV x-ray pulse (2).
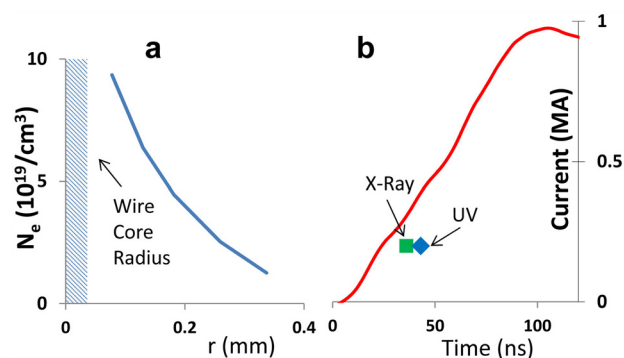

FIG. 7. (a) The electron plasma density calculated from the interferogram in shot #3357 with an Al 8-wire cylindrical array, 18 mm in diameter. (b) The timing diagram with a current pulse and the UV and x-ray frames in this shot.
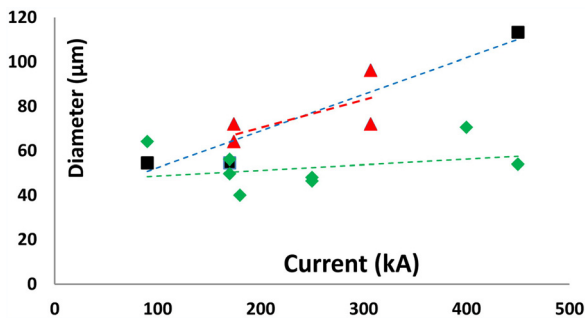
FIG. 8. Wire core diameters as a function of current for a number of shots. Shown are data point for an eight 15-μm Al wires in cylindrical loads 8 mm in diameter (squares), and the outer wires (triangles) and inner wires (diamonds) of a 3-ray 12-wire Al star load, 20 and 15 μm in diameter.

density up to 80 μm from the wire center, measuring a peak plasma density of 9.6×10^{19} cm^{-3}. The X-ray imaging measures the radius of the dense wire core at ~40 μm. A spatial resolution was measured by the method presented in Ref. 34. The spread of the image of the wire edge is measured at 18 μm. This resolution does not allow investigation of the fine structure of the wire core but the expansion of the core during the ablation stage can be measured in a wide range of current. Figure 7 demonstrates that two diagnostics, laser probing and X-ray imaging provide complementary measurements of the plasma density and core size in the Al wire array at the ablation stage.

Figure 8 shows the expansion velocity of outermost wires in the Al star and cylindrical wire arrays at the ablation stage. It was revealed that wire core diameter expanded to 3–5 times initial wire diameter in the ablation stage. The diagram shows the average wire core radius at different current levels during the ablation stage up to the beginning of implosion. The experiments were performed with Al wires in two types of loads: cylindrical, 18 mm in diameter, and star loads with 3-rays, 12 or 15 wires 15–20 μm in diameter placed on diameters 20/18.5/17/14/6 mm. The outer wires in the star arrays and wires in cylindrical loads experienced similar wire core diameter and growth rates, measured at ~1.5 μm/ns. The variation of the initial wire size variation in the range of 15–25 μm showed little change in the wire core diameter or expansion rates, suggesting that the wire core size has low sensitivity to the initial wire diameter. However, inner wires in the star wire array experienced little to no growth as the current increased. This is not an unexpected result, due to the "cascading" implosion seen in star wire arrays, where the inner wires remain with a small level of ablation until the outer wires implode and collide with them. This is a result of inductance splitting of the current, which causes a majority of the current on the outer wires in the wire array. After the collision, the next wire from the edge is subjected to higher current, ablates fast, and begins the implosion to the next wire.

IV. CONCLUSION

Plasma in the ablating wire is opaque for regular laser diagnostics in the optical range. UV diagnostics combined with X-ray radiography provides information for a wide range of densities of the plasma corona and non-plasma core

in wire arrays at the ablating stage. The interferometry at the wavelength of 266 nm is capable of directly measuring electron densities as high as 2×10^{20} cm^{-3} in the ablating wires and "fingers" in the imploding plasma. The evolution of the plasma density profile of the Al wire corona is measured with 2-frame interferometry, and a total mass of the plasma column of the wire can be estimated from interferograms. Two-frames of interferometry in one shot with a 7 ns delay between frames shows an example when 36% and 72% of the initial mass of the 12.7 μm Al wire are contained in the plasma column at the later ablation stage. By this way, the interferometry can be used for estimation of the effective ion ionization in the wire plasma column if the ablated mass is calculated by the rocket model.[35] UV diagnostics allow the investigation of the ablating plasma column in low-atomic-number elements which are too transparent for X-ray backlighting.

During the implosion stage, the interferometry is appropriate for studying the electron plasma density in the trailing mass left behind by the implosion front. The interferometry at 266 nm is capable of measuring both the plasma of dense "fingers" and the gaps located between them. The gaps are filled with a lower density plasma, which provides a current path in the non-imploded plasma. This allows for the J × B force to accelerate the rest of plasma to the Z pinch.

UV Faraday rotation diagnostics at 266 nm reveal local magnetic fields and can be used to determine the local current distribution of the Z pinch.[9] The Faraday effect was used to measure the magnetic field and estimate current in the imploding plasma of the Al star wire array. The plasma electron density and rotation angle were measured from the shadowgram, interferogram, and their reference images. Abel inversion was applied to reconstruct the electron density and magnetic field radial profile in the imploding plasma. In the 3-ray star array, the imploding plasma is accumulated in three plasma columns at positions of three inner wires before the final implosion.[29] The maximum magnetic field of 1.3 MG was measured in the plasma column at this stage. The magnetic field in plasma was compared with a simple model of uniform current flowing in a plasma column. The model fits experimental data if a radius of the plasma column is 0.9 mm and $I = 0.3$ MA in a single column. This current is in agreement with a total current of 0.94 MA in the Z pinch measured by B-dots at this time.

The dense non-plasma wire core seen during the ablation stage of the Z pinch is opaque to UV laser probing, motivating the development of a complementary X-ray imaging diagnostic. The surrounding Al plasma is transparent to the X-ray imaging in the keV range, revealing the underlying dense non-plasma core. Coupled with UV laser diagnostics, X-ray imaging radiography was used to deliver experimental data for both the core and corona in one shot. The laser-based radiography allows measuring the core size in a wide range of delays up to the beginning of implosion. The expansion velocity of the core in the star arrays and wires in cylindrical loads was measured at ~1.5 μm/ns. Different dynamics of wire cores in star and cylindrical loads are in agreement with data from laser diagnostics. Inner wires in the star load showed little or no growth up to the

moment when the core of the external wire disappeared. This dynamic is consistent with the cascading implosion dynamics in star wire arrays.

UV laser diagnostics at the wavelength of 266 nm allow investigation of many features in wire-array plasma at the 1 MA Zebra generator. Development of laser diagnostics to the deep UV range[26] will help to penetrate deeper in the Z pinch plasma using well established optical methods for measurement of the electron density, gradients, and magnetic fields in dense plasma.

ACKNOWLEDGMENTS

[1]C. Deeney, R. Douglas, R. B. Spielman, T. J. Nash, D. L. Peterson, P. L'Eplattenier, G. A. Chandler, J. F. Seaman, and K. W. Struve, Phys. Rev. Lett. **81**, 4883 (1998).

[2]R. B. Spielman, C. Deeney, G. A. Chandler, M. R. Douglas, D. L. Fehl, M. K. Matzen, D. H. McDaniel, T. J. Nash, J. L. Porter, T. W. L. Sanford, J. F. Seamen, W. A. Stygar, K. W. Struwe, S. P. Breeze, J. S. McGurn, J. A. Torres, D. M. Zagar, T. L. Gilliland, D. O. Job, J. L. McKenney, R. C. Mock, M. Vargas, and T. Wagoner, Phys. Plasmas **5**, 2105 (1998).

[3]T. W. L. Sanford, C. A. Jennings, G. A. Rochau, S. E. Rosenthal, G. S. Sarkisov, P. V. Sasorov, W. A. Stygar, L. F. Bennett, D. E. Bliss, J. P. Chittenden, M. E. Cuneo, M. G. Haines, R. J. Leeper, R. C. Mock, T. J. Nash, and D. L. Peterson, Phys. Plasmas **14**, 052703 (2007).

[4]M. E. Cuneo, E. M. Wasiman, S. V. Lebedev, J. P. Chittenden, W. A. Stygar, G. A. Chandler, R. A. Vesey, E. P. Yu, T. J. Nash, D. E. Bliss, G. S. Sarkisov, T. C. Wagoner, G. R. Bennett, D. B. Sinars, J. L. Porter, W. W. Simpson, L. E. Ruggles, D. F. Wenger, C. J. Garasi, B. V. Oliver, R. A. Aragon, W. E. Fowler, M. C. Hettrick, G. C. Idzorek, D. Johnson, K. Keller, S. E. Lazier, J. S. McGurn, T. A. Mehlhorn, T. Moore, D. S. Nielsen, J. Pyle, S. Speas, K. W. Struve, and J. A. Torres, Phys. Rev. E **71**, 046406 (2005).

[5]B. A. Remington, R. P. Drake, and D. D. Ryutov, Rev. Mod. Phys. **78**, 755 (2006).

[6]S. V. Lebedev, I. H. Mitchell, R. Aliaga-Rossel, S. N. Bland, J. P. Chittenden, A. E. Dangor, and M. G. Haines, Phys. Rev. Lett. **81**, 4152 (1998).

[7]D. B. Sinars, M. E. Cuneo, E. P. Yu, D. E. Bliss, T. J. Nash, J. L. Porter, C. Deeney, M. G. Mazarakis, G. S. Sarkisov, and D. F. Wenger, Phys. Rev. Lett. **93**, 145002 (2004).

[8]V. V. Ivanov, J. P. Chittenden, S. D. Altemara, N. Niasse, P. Hakel, R. C. Mancini, D. Papp, and A. A. Anderson, Phys. Rev. Lett. **107**, 165002 (2011).

[9]V. V. Ivanov, J. P. Chittenden, R. C. Mancini, D. Papp, N. Niasse, S. D. Altemara, and A. A. Anderson, Phys. Rev. E **86**, 046403 (2012).

[10]S. V. Lebedev, F. N. Beg, S. N. Bland, J. P. Chittenden, A. E. Dangor, M. G. Haines, S. A. Pikuz, and T. A. Shelkovenko, Phys. Rev. Lett. **85**, 98 (2000).

[11]S. A. Pikuz, T. A. Shelkovenko, D. B. Sinars, J. B. Greenly, Y. S. Dimant, and D. A. Hammer, Phys. Rev. Lett. **83**, 4313 (1999).

[12]S. V. Lebedev, F. N. Beg, S. N. Bland, J. P. Chittenden, A. E. Dangor, M. G. Haines, M. Zakaullah, S. A. Pikuz, T. A. Shelkovenko, and D. A. Hammer, Rev. Sci. Instrum. **72**, 671 (2001).

[13]E. V. Grabovskii, K. N. Mitrofanov, G. M. Oleinik, and I. Yu. Porofeev, Plasma Phys. Rep. **30**, 121 (2004).

[14]V. V. Ivanov, V. I. Sotnikov, G. S. Sarkisov, T. E. Cowan, S. N. Bland, B. Jones, C. A. Coverdale, C. Deeney, P. J. Laca, A. L. Astanovitskiy, and A. Haboub, Phys. Rev. Lett. **97**, 125001 (2006).

[15]G. F. Swadling, S. V. Lebedev, N. Niasse, J. P. Chittenden, G. N. Hall, F. Suzuki-Vidal, G. Burdiak, A. J. Harvey-Thompson, S. N. Bland, P. De Grouchy, E. Khoory, L. Pickworth, J. Skidmore, and L. Suttle, Phys. Plasmas **20**, 022705 (2013).

[16]V. V. Ivanov, V. I. Sotnikov, G. S. Sarkisov, A. L. Astanovitskiy, P. J. Laca, T. E. Cowan, B. Jones, C. Deeney, B. V. Oliver, T. A. Mehlhorn, and J. G. Leboeuf, IEEE Trans. Plasma Sci. **35**, 1170 (2007).

[17]D. J. Ampleford, B. Jones, S. C. Bott, S. V. Lebedev, S. N. Bland, G. N. Hall, and J. B. A. Palmer, IEEE Trans. Plasma Sci. **36**, 1270 (2008).

[18]S. E. Pikuz, T. A. Shelkovenko, A. R. Mingaleev, D. A. Hammer, and H. P. Neves, Phys. Plasmas **6**, 4272 (1999).

[19]J. D. Douglass, D. A. Hammer, S. A. Pikuz, T. A. Shelkovenko, and K. S. Blesener, Phys. Plasmas **19**, 072710 (2012).

[20]V. V. Ivanov, P. Hakel, R. C. Mancini, J. P. Chittenden, A. A. Anderson, T. Durmaz, P. P. Wiewior, D. Papp, S. D. Altemara, A. L. Astanovitskiy, and O. Chalyy, Phys. Rev. Lett. **106**, 225005 (2011).

[21]P. F. Knapp, S. A. Pikuz, T. A. Shelkovenko, D. A. Hammer, and S. B. Hansen, Phys. Plasmas **19**, 056302 (2012).

[22]V. V. Ivanov, V. I. Sotnikov, J. M. Kindel, P. Hakel, R. C. Mancini, A. L. Astanovitskiy, A. Haboub, S. D. Altemara, A. P. Shevelko, E. D. Kazakov, and P. V. Sasorov, Phys. Rev. E **79**, 056404 (2009).

[23]W. Lochte-Holtgreven, *Plasma Diagnostics*, American Vacuum Society Classics, edited by H. F. Dylla (AIP, New York, NY, USA, 1995).

[24]V. V. Ivanov, S. D. Altemara, A. A. Astanovitskiy, G. S. Sarkisov, A. Haboub, D. Papp, and J. M. Kindel, IEEE Trans. Plasma Sci. **38**, 574 (2010).

[25]G. S. Sarkisov, Instrum. Exp. Tech. **39**, 727 (1996).

[26]V. V. Ivanov, A. A. Anderson, D. Papp, B. R. Talbot, J. P. Chittenden, N. Niasse, and I. A. Begishev, IEEE Trans. Plasma Sci. **42**, 1153 (2014).

[27]V. V. Ivanov, P. Hakel, R. C. Mancini, J. P. Chittenden, A. Anderson, A. P. Shevelko, P. Wiewior, T. Durmaz, S. D. Altemara, D. Papp, A. L. Astanovitskiy, V. Nalajala, O. Chalyy, and O. Dmitriev, HEDP **7**, 383–390 (2011).

[28]P. P. Wiewior, V. V. Ivanov, and O. Chalyy, J. Phys.: Conf. Ser. **244**, 032013 (2010).

[29]D. B. Sinars, G. R. Bennett, D. F. Wenger, M. E. Cuneo, and J. L. Porter, Appl. Opt. **42**, 4059 (2003).

[30]V. V. Ivanov, V. I. Sotnikov, A. Haboub, A. P. Shevelko, A. L. Astanovitskiy, A. Morozov, E. D. Kazakov, and S. D. Altemara, Phys. Rev. Lett. **100**, 025004 (2008).

[31]C. Deeney, T. Nash, R. R. Prasad, L. Warren, K. G. Whitney, J. W. Thornhill, and M. C. Coulter, Phys. Rev. A **44**, 6762 (1991).

[32]A. L. Velikovich, J. Davis, J. W. Thornhill, J. L. Guilliani Jr., L. I. Rudakov, and C. Deeney, Phys. Plasmas **7**, 3265 (2000).

[33]V. V. Ivanov, A. A. Anderson, D. Papp, A. L. Astanovitskiy, B. R. Talbot, J. P. Chittenden, and N. Niasse, Phys. Rev. E **88**, 013108 (2013).

[34]P. F. Knapp, S. A. Pikuz, T. A. Shelkovenko, D. A. Hammer, and S. B. Hansen, Rev. Sci. Instrum. **82**, 063501 (2011).

[35]S. V. Lebedev, F. N. Beg, S. N. Bland, J. P. Chittenden, A. E. Dangor, and M. G. Haines, Phys. Plasmas **9**, 2293 (2002).